PHOTONICS Research

Concise and efficient direct-view generation of arbitrary cylindrical vector beams by a vortex half-wave plate

Junli Qi,[1,2,3,4] Weihua Wang,[1,2,5,6] Bo Shi,[4] Hui Zhang,[4] Yanan Shen,[4] Haifei Deng,[4] Wenjing Pu,[4] Xin Liu,[4] Huihui Shan,[4] Xiaomin Ma,[4] Lianqiang Zhang,[4] Wei Lu,[5] Meicheng Fu,[3] [iD] and Xiujian Li[3,7]

[1]*Institute of Plasma Physics, Hefei Institutes of Physical Sciences, Chinese Academy of Sciences, Hefei 230031, China*
[2]*Science Island Branch of Graduate School, University of Science and Technology of China, Hefei 230031, China*
[3]*College of Liberal Arts and Sciences, National University of Defense Technology, Changsha 410073, China*
[4]*Institute of Applied Physics, Army Academy of Artillery and Air Defense, Hefei 230031, China*
[5]*Institute of Physical Science and Information Technology, Anhui University, Hefei 230031, China*
[6]*e-mail: whwang@ipp.ac.cn*
[7]*e-mail: xjli@nudt.edu.cn*

A concise, efficient, and practical direct-view scheme is presented to generate arbitrary cylindrical vector (CV) beams, including CV beams, vortex beams, and cylindrical vector vortex (CVV) beams, by a vortex half-wave plate (VHP). Six kinds of first-order and other high-order CV beams, such as azimuthally polarized (AP) beams, anti-vortex radial polarization mode beams, and three-order AP beams, are formed by simply rotating a half-wave plate. The Stokes parameters and double-slit interference of multitype CV beams are investigated in detail. The polarization parameters, including degree of polarization, polarization azimuth, and ellipticity, are obtained, which demonstrates the efficient generation of CV beams. In addition, the double-slit interference experiment is introduced in the setup, and fringe misplacement and tilt appear for CVV beams, in which the misplacement number M is $2P + 1$ for $P \leq 2$ and $2P - 1$ for $P \geq 3$, where P is the polarization order number, and the fringe tilt offset is positively related to the topological charge number l of CVV beams. In addition, new types of VHPs can be formed by cascading two or more VHPs when the types of available VHPs are limited, assisting in more flexible generation of multitype CV beams. It is experimentally demonstrated that arbitrary CV beams with high quality are effectively achieved by the proposed setup, and the double-slit interference method can be utilized to determine and analyze CV beams rapidly and concisely by practical performance, which shows the potential to be implemented as a commercial device.   © 2021 Chinese Laser Press

https://doi.org/10.1364/PRJ.419561

1. INTRODUCTION

With a cylindrically symmetric intensity profile and a variable polarization endowed with a vortex phase about the beam axis, cylindrical vector (CV) beams have attracted widespread attention [1,2]. As a typical representative of CV beams, the radially polarized (RP) and azimuthally polarized (AP) beams have been found to have important applications in the fields such as tight focusing [3–5], beam shaping [6–9], particle accelerating and trapping [10–14], laser materials processing [15–17], superresolution techniques [18–20], and optical metrology [21–23]. Recent studies have also demonstrated potential applications of CV beams in optical communication [24–26], quantum information processing [27–29], spin and orbital angular momentum effects [30–34], inverse energy flux [35,36], plasmonic nanostructures [37,38], and fiber and integrated optics [39–42].

Various techniques and schemes have been developed to generate CV beams. Generally, these methods can be categorized into two classes: intracavity (active) and external conversion (passive) [1]. The intracavity method is to generate CV beams directly in the laser by putting in special optical elements; the internal structure of the laser needs to be adjusted accordingly, including the use of crystal birefringence [43–45], Brewster angle characteristics [46,47], cavity configuration design [48], and geometric phase control [49]. These methods can generate vector beams with high quality and energy conversion efficiency but lack flexibility due to limited space and complex technology to reconstruct the existing laser. The external conversion method refers to transforming spatially uniform polarized beams into CV beams through certain phase devices or decomposition and recombination outside the laser. The commonly used external devices include segmented spiral

varying retarders [50–52], special phase plates [53,54], anisotropic crystals [55–58], diffractive optical elements [59,60], subwavelength gratings [61–63], and metasurfaces [64–67]. However, these conversion methods have the problems of low conversion efficiency and high design cost. Interferometric devices have also been proposed to generate CV beams, such as Sagnac interferometers [68–71], Mach–Zehnder interferometers [72,73], and other interferometers [74–78]. But the interferometric methods often need high stability and precise control, which reduces conversion efficiency and accuracy. Nowadays, the spatial light modulator (SLM) is mostly used to realize CV beams, including the double SLM method [79–82] and split-screen method by a single SLM [83–88]. However, the double SLM method is not cost-effective, and the split-screen method has the drawback of low SLM area utility. In addition, due to the diffraction effect, the SLM method has low conversion efficiency and cannot withstand high-energy laser beams because of the liquid crystal material.

Herein, we demonstrate a concise, efficient, and practical direct-view method to generate arbitrary CV beams by vortex half-wave plate (VHP) without beam reflection and deflection, including realizing CV beams, vortex beams, and CVV beams. The VHP is a special half-wave plate (HP) with a consistent delay π, but the direction of the fast axis changes continuously around the circle center. It has high transmittance just like an HP, so it has high energy utilization and can be made up to 2 inches, which can realize the conversion of high-energy beams through beam expansion and recompression. In addition, new types of VHPs can be formed by cascading two or more VHPs when the types of available VHPs are limited, which helps in more flexible generation of multitype CV beams.

In this paper, six kinds of first-order and other high-order CV beams, such as the RP beam, AP beam, and three-order AP beam, are formed by simply rotating an HP. The Stokes parameters and double-slit interference of multitype CV beams are investigated in detail. The polarization parameters, including degree of polarization (DOP), polarization azimuth, and ellipticity, are obtained, which demonstrates the efficient generation of the CV beams. Additionally, misplacement and tilt appear in the double-slit interference fringes of CVV beams, in which the misplacement number M is $2P + 1$ for $P \leq 2$ and $2P - 1$ for $P \geq 3$, where P is the polarization order number, and the fringe tilt offset is positively related to the topological charge number l of the CVV beams. It is experimentally demonstrated that arbitrary CV beams with high quality are effectively achieved by the proposed setup, and the double-slit interference method can be utilized to determine and analyze CV beams rapidly and concisely through practical performance.

2. PRINCIPLES

A. VHP
The VHP is a special HP that is made of liquid crystal polymer with birefringence. It has a consistent delay π, with the direction of the fast axis changing continuously around the circle center. The distribution of the fast axis can be described as the following:

$$\theta = \frac{m}{2}\psi + \sigma, \tag{1}$$

where ψ is the VHP azimuth angle, θ is the VHP fast axis direction at a certain azimuth angle, m is the order number, and σ is the fast axis direction when $\psi = 0$. The VHP with m and σ will be expressed as VHP(m, σ) for short in the following. The fast axis distributions of several VHPs with $\sigma = 0$ and $m = 1$, 2, 3, 4, respectively, are shown in Fig. 1.

The VHP Jones matrix $J_{m,\sigma}$ with fast axis at the direction θ can be expressed as

$$J_{m,\sigma} = \begin{bmatrix} \cos 2\theta & \sin 2\theta \\ \sin 2\theta & -\cos 2\theta \end{bmatrix}$$

$$= \begin{bmatrix} \cos(m\psi + 2\sigma) & \sin(m\psi + 2\sigma) \\ \sin(m\psi + 2\sigma) & -\cos(m\psi + 2\sigma) \end{bmatrix}, \tag{2}$$

in which θ varies with the azimuth angle ψ, so that the VHP Jones matrix is spatially variable. For VHPs with the same order number m but different σ (except for $m = 2$), they can be converted to each other by rotation. To convert the m-order VHP with $\sigma = 0$ to the same order VHP with $\sigma = \phi$, the clockwise rotation angle Φ can be expressed as follows:

$$\frac{m}{2}\Phi - \Phi = \phi \Rightarrow \Phi = \frac{2\phi}{m - 2}. \tag{3}$$

When Φ is a negative value, it represents an anti-clockwise rotation, and a positive value denotes a clockwise rotation. Taking the first-order and fourth-order VHPs as examples, the VHP(1, 0) can be converted to VHP(1, $\pi/12$) by rotating 30° anti-clockwise. Similarly, the VHP(4, 0) becomes VHP(4, $\pi/6$) by rotating 30° clockwise. And the VHP(4, $-\pi/6$) (or $\sigma = 5\pi/6$) will be obtained by rotating the VHP(4, 0) by 30° anti-clockwise.

B. Generation of CV Vector Beams
We will take the VHP with $m = 1$ to generate arbitrary first-order CV beams, for example. When the incident beam is horizontally polarized with the Jones vector $E_{//} = [1 \quad 0]^T$, for the VHP(1, 0), the Jones vector of the transmitted beam is expressed as

$$E_{RP} = J_{1,0} \cdot E_{//} = \begin{bmatrix} \cos\psi & \sin\psi \\ \sin\psi & -\cos\psi \end{bmatrix} \cdot \begin{bmatrix} 1 \\ 0 \end{bmatrix} = \begin{bmatrix} \cos\psi \\ \sin\psi \end{bmatrix}, \tag{4}$$

which is the RP beam. When the horizontally polarized beam passes through the VHP(1, $\pi/4$), the Jones vector of the transmitted beam is expressed as

$$E_{AP} = J_{1,\pi/4} \cdot E_{//} = \begin{bmatrix} \cos(\psi + \pi/2) \\ \sin(\psi + \pi/2) \end{bmatrix} = \begin{bmatrix} -\sin\psi \\ \cos\psi \end{bmatrix}, \tag{5}$$

which is the AP beam, i.e., on the basis of radial polarization, each polarization direction is rotated 90° anti-clockwise. Or, with the vertically polarized beam input, with the Jones vector
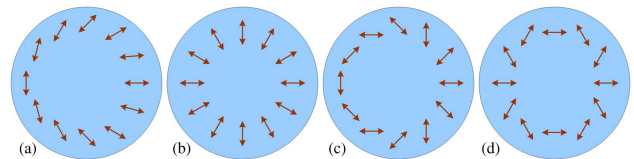
Fig. 1. Fast axis distributions of several VHPs with $\sigma = 0$. (a)–(d) are the distributions with $m = 1$, 2, 3, 4, respectively.

$E_\perp = [0 \quad 1]^T$ for the VHP(1, 0), the Jones vector of the transmitted beam is expressed as

$$E'_{AP} = J_{1,0} \cdot E_\perp = \begin{bmatrix} \sin\psi \\ -\cos\psi \end{bmatrix} = \begin{bmatrix} \cos(\psi - \pi/2) \\ \sin(\psi - \pi/2) \end{bmatrix}$$
$$= e^{i\pi} \cdot E_{AP}, \tag{6}$$

which is still the AP beam, but each polarization direction is rotated 90° clockwise on the basis of radial polarization. Compared with the previous case, there is only a π-phase difference. If the horizontally polarized beam is input, for the VHP $(1, \pi/8)$, the Jones vector of the transmitted beam is expressed as

$$E^1_{\pi/4} = J_{1,\pi/8} \cdot E_{//} = \begin{bmatrix} \cos(\psi + \pi/4) \\ \sin(\psi + \pi/4) \end{bmatrix}. \tag{7}$$

It means that each polarization direction is rotated 45° anti-clockwise on the basis of radial polarization, which is called the first-order $\pi/4$-CV beam. The superscript 1 in $E^1_{\pi/4}$ represents polarization order number $P = 1$ of CV beams. Also, $E^1_{-\pi/4}$ can be obtained by inputting a horizontally polarized beam for the VHP(1, $-\pi/8$) or VHP(1, $3\pi/8$) as the following:

$$E^1_{-\pi/4} = J_{1,-\pi/8} \cdot E_{//} = \begin{bmatrix} \cos(\psi - \pi/4) \\ \sin(\psi - \pi/4) \end{bmatrix}$$
$$= e^{i\pi} \cdot \begin{bmatrix} \cos(\psi + 3\pi/4) \\ \sin(\psi + 3\pi/4) \end{bmatrix} = e^{i\pi} \cdot J_{1,3\pi/8} \cdot E_{//}. \tag{8}$$

We can get multitype CV beams by directly rotating the VHP with $\sigma = 0$ when the horizontally or vertically polarized beam is input. But this method cannot obtain other second-order CV beams except for the second-order RP beam, and with the increase of order m, the rotation angle of VHP becomes smaller, and the accuracy will be more difficult to control. Taking the high-order AP beam (requiring $\phi = \pm\pi/4$) as an example, according to Eq. (3), the rotation angle Φ of VHP with $\sigma = 0$ is $\Phi = \pm\pi/[2(m - 2)]$. Obviously, the larger the order m (for $m \geq 3$) is, the smaller the rotation angle ϕ of VHP with $\sigma = 0$ becomes, and the higher rotation accuracy is needed.

So, the method of changing the polarization direction of an incident linearly polarized beam by rotating an HP to generate CV beams is proposed without rotating the VHP. And the polarization direction of the incident beam need not change with the increase of the order m for generating the same kind of other high-order CV beams. When the incident beam is a linearly polarized one, with the polarization direction orientated at α according to the horizontal direction (x axis) for the VHP(m, 0), the Jones vector of the transmitted beam is expressed as the following:

$$E^m_{-\alpha} = J_{m,0} \cdot E_\alpha = \begin{bmatrix} \cos(m\psi) & \sin(m\psi) \\ \sin(m\psi) & -\cos(m\psi) \end{bmatrix} \cdot \begin{bmatrix} \cos\alpha \\ \sin\alpha \end{bmatrix}$$
$$= \begin{bmatrix} \cos(m\psi - \alpha) \\ \sin(m\psi - \alpha) \end{bmatrix}. \tag{9}$$

This means that each polarization direction is rotated by $-\alpha$ anti-clockwise on the basis of the radial polarization. The superscript m in $E^m_{-\alpha}$ represents polarization order number $P = m$ of

the CV beams. So, the $E_{RP}, E_{AP}, E^m_{\pi/4}, E^m_{-\pi/4}$ can be obtained when $\alpha = 0, -\pi/2, -\pi/4,$ and $\pi/4$, respectively.

In addition, when the RP beam passes through an HP with the fast axis in the horizontal (or vertical) direction, i.e., 0° HP (or 90° HP) with the Jones matrix described as J_0 (or $J_{\pi/2} = e^{i\pi} \cdot J_0$), the Jones vector of the transmitted beam is expressed as

$$E_{ARP} = J_0 \cdot E_{RP} = \begin{bmatrix} 1 & 0 \\ 0 & -1 \end{bmatrix} \cdot \begin{bmatrix} \cos\psi \\ \sin\psi \end{bmatrix} = \begin{bmatrix} \cos(-\psi) \\ \sin(-\psi) \end{bmatrix}. \tag{10}$$

That is, the polarization direction at the azimuth angle ψ is $-\psi$, which is called anti-vortex radial polarization (ARP) [89] or quasi-radial polarization (q-RP) [90] mode with the polarization order number $P = -1$. When the AP beam passes through the 0° HP, or the RP beam passes through an HP with the fast axis at 45° direction with the Jones matrix $J_{\pi/4}$, the Jones vector of the transmitted beam is expressed as

$$E_{AAP} = J_0 \cdot E'_{AP} = J_{\pi/4} \cdot E_{RP} = \begin{bmatrix} 0 & 1 \\ 1 & 0 \end{bmatrix} \cdot \begin{bmatrix} \cos\psi \\ \sin\psi \end{bmatrix}$$
$$= \begin{bmatrix} \sin\psi \\ \cos\psi \end{bmatrix} = \begin{bmatrix} \cos(-\psi + \pi/2) \\ \sin(-\psi + \pi/2) \end{bmatrix}. \tag{11}$$

The polarization direction is $-\psi + \pi/2$ at the azimuth angle ψ, which is called the anti-vortex azimuthal polarization (AAP) or quasi-azimuth polarization (q-AP) mode. For instance, in the direction of azimuth angle $\psi = 0°$, the polarization direction is 90°, at $\psi = 45°$, the polarization direction is 45°, and at $\psi = 135°$, the polarization direction is $-45°$. In the same azimuth direction, the polarization direction of the AAP mode is that of the ARP mode rotated 90° anti-clockwise.

The polarization distributions of all the above CV beams are shown in Fig. 2. Figures 2(a)–2(f) represent the polarization and intensity distributions of $E_{RP}, E_{AP}, E^1_{\pi/4}, E^1_{-\pi/4}, E_{ARP}, E_{AAP}$, respectively.

The high-order CV beams will be obtained when a linearly polarized beam passes through the VHP with $m \geq 2$.

C. Generation of Vortex Beams

The Jones matrix of a quarter-wave plate (QP) with fast axis in θ direction relative to the horizontal direction (x axis) is expressed as follows:

$$J_\theta^{(\lambda/4)} = \frac{\sqrt{2}}{2} \begin{bmatrix} 1 - i\cos 2\theta & -i\sin 2\theta \\ -i\sin 2\theta & 1 + i\cos 2\theta \end{bmatrix}. \tag{12}$$

When the horizontally polarized beam passes through the QPs with fast axis in 45° and $-45°$ direction, respectively, right-handed and left-handed circularly polarized beams will be obtained with the corresponding Jones vectors described as $E_R = \sqrt{2}/2[1 \quad -i]^T$ and $E_L = \sqrt{2}/2[1 \quad i]^T$.
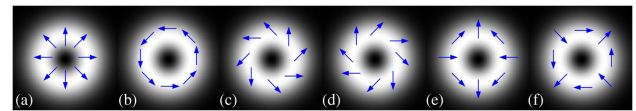
Fig. 2. Polarization distributions of various one-order CVP beams. (a)–(f) correspond to the polarization distributions of $E_{RP}, E_{AP}, E^1_{\pi/4}, E^1_{-\pi/4}, E_{ARP}, E_{AAP}$.

The VHP(m, σ) can transform an incident circularly polarized beam into a vortex wavefront. When the incident beam is left-handed circularly polarized, the transmitted beam is a vortex one with the topological charge number $l = m$, and the polarization state becomes right-handed circularly polarized. The corresponding Jones vector is as follows:

$$J_{m,\sigma} \cdot E_L = \frac{\sqrt{2}}{2} \begin{bmatrix} \cos 2\theta + i \sin 2\theta \\ \sin 2\theta - i \cos 2\theta \end{bmatrix} = \frac{\sqrt{2}}{2} \begin{bmatrix} e^{i2\theta} \\ e^{i(2\theta - \pi/2)} \end{bmatrix}$$

$$= \frac{\sqrt{2}}{2} \begin{bmatrix} 1 \\ -i \end{bmatrix} \cdot e^{i(m\psi + 2\sigma)} = E_R \cdot e^{i(m\psi + 2\sigma)} = E_{ARCV},$$

$$(13)$$

which is an anti-clockwise vortex beam with right-handed circular polarization, i.e., anti-clockwise right-handed circularly-polarized vortex (ARCV) beam. 2σ is only an initial fixed phase and does not affect the relative phase distribution of the whole vortex beam.

When the incident beam is a right-handed circularly polarized beam, the exit beam is a vortex beam with topological charge number $l = -m$, and the polarization state becomes left-handed circularly polarized. The corresponding Jones vector is as follows:

$$J_{m,\sigma} \cdot E_R = \frac{\sqrt{2}}{2} \begin{bmatrix} \cos 2\theta - i \sin 2\theta \\ \sin 2\theta + i \cos 2\theta \end{bmatrix} = \frac{\sqrt{2}}{2} \begin{bmatrix} e^{i(-2\theta)} \\ e^{i(-2\theta + \pi/2)} \end{bmatrix}$$

$$= \frac{\sqrt{2}}{2} \begin{bmatrix} 1 \\ i \end{bmatrix} \cdot e^{-i(m\psi + 2\sigma)} = E_L \cdot e^{-i(m\psi + 2\sigma)}$$

$$= E_{CLCV},$$

$$(14)$$

which is the clockwise vortex beam with left-handed circular polarization, i.e., clockwise left-handed circularly polarized vortex (CLCV) beam.

D. Generation of CVV Beams

When the circularly polarized vortex beam passes through a QP with the fast axis in 45° or −45° direction, it can be converted into a linearly-polarized vortex (LV) beam. The conversion process of the Jones vector is as follows:

$$J_{\pi/4}^{(\lambda/4)} \cdot E_{ARCV} = \begin{bmatrix} 0 \\ -i \end{bmatrix} \cdot e^{i(m\phi + 2\sigma)} = E_\perp \cdot e^{i(m\psi + 2\sigma - \pi/2)} = E_{AVLV},$$

$$J_{-\pi/4}^{(\lambda/4)} \cdot E_{ARCV} = \begin{bmatrix} 1 \\ 0 \end{bmatrix} \cdot e^{i(m\phi + 2\sigma)} = E_{//} \cdot e^{i(m\psi + 2\sigma)} = E_{AHLV}.$$

$$(15)$$

An anti-clockwise vertically linearly polarized vortex (AVLV) beam is obtained when the ARCV beam passes through the QP

with the fast axis at 45°, and an anti-clockwise horizontally linearly polarized vortex (AHLV) beam is obtained when the ARCV beam passes through the QP with the fast axis at −45°.

Similarly, when the CLCV beam passes through the QP with the fast axis at 45°, a clockwise horizontally linearly polarized vortex (CHLV) beam is obtained. And a clockwise vertically linearly polarized vortex (CVLV) beam is obtained when the CLCV beam passes through the QP with the fast axis at −45°. The conversion process of Jones vector is as follows:

$$J_{\pi/4}^{(\lambda/4)} \cdot E_{CLCV} = \begin{bmatrix} 1 \\ 0 \end{bmatrix} \cdot e^{-i(m\phi + 2\sigma)} = E_{//} \cdot e^{-i(m\psi + 2\sigma)} = E_{CHLV},$$

$$J_{-\pi/4}^{(\lambda/4)} \cdot E_{CLCV} = \begin{bmatrix} 0 \\ i \end{bmatrix} \cdot e^{-i(m\phi + 2\sigma)} = E_\perp \cdot e^{-i(m\psi + 2\sigma - \pi/2)} = E_{CVLV}.$$

$$(16)$$

Combined with Section 2.B, it is easy to find that a CVV beam can be obtained when a generated LV beam passes through another VHP. The corresponding Jones vector is depicted as follows:

$$J_{m_2,\sigma_2} \cdot E_{AHLV} = \begin{bmatrix} \cos(m_2\psi + 2\sigma_2) \\ \sin(m_2\psi + 2\sigma_2) \end{bmatrix} \cdot e^{i(m_1\psi + 2\sigma_1)} = E_{R_{m_2} V_{m_1}},$$

$$J_{m_2,\sigma_2} \cdot E_{AVLV} = \begin{bmatrix} \sin(m_2\psi + 2\sigma_2) \\ -\cos(m_2\psi + 2\sigma_2) \end{bmatrix} \cdot e^{i(m_1\psi + 2\sigma_1 - \pi/2)} = E_{A_{m_2} V_{m_1}}.$$

$$(17)$$

The m_2-order radially polarized vortex (RPV) beam with topological charge number $l = m_1$ is generated when the AHLV beam with $l = m_1$ passes through the second m_2-order VHP with $\sigma = 0$. Similarly, an m_2-order azimuthally polarized vortex (APV) beam with $l = m_1$ is generated when the CVLV beam with $l = m_1$ passes through the second m_2-order VHP with $\sigma = 0$. The conversion process of Jones vector is as follows:

$$J_{m_2,\sigma_2} \cdot E_{CHLV} = \begin{bmatrix} \cos(m_2\psi + 2\sigma_2) \\ \sin(m_2\psi + 2\sigma_2) \end{bmatrix} \cdot e^{-i(m_1\psi + 2\sigma_1)} = E'_{R_{m_2} V_{m_1}},$$

$$J_{m_2,\sigma_2} \cdot E_{CVLV} = \begin{bmatrix} \sin(m_2\psi + 2\sigma_2) \\ -\cos(m_2\psi + 2\sigma_2) \end{bmatrix} \cdot e^{-i(m_1\psi + 2\sigma_1 - \pi/2)} = E'_{A_{m_2} V_{m_1}}.$$

$$(18)$$

E. Increasing Types of VHP

New types of VHPs can be formed by cascading two or more VHPs when the types of available VHPs are limited. The cascading of two and three VHPs is described, respectively, in detail. The combined Jones matrix of two VHPs can be expressed as

$$J_2 \cdot J_1 = J_{m_2,\sigma_2} \cdot J_{m_1,\sigma_1} = \begin{bmatrix} \cos \alpha_2 & \sin \alpha_2 \\ \sin \alpha_2 & -\cos \alpha_2 \end{bmatrix} \cdot \begin{bmatrix} \cos \alpha_1 & \sin \alpha_1 \\ \sin \alpha_1 & -\cos \alpha_1 \end{bmatrix}$$

$$= \begin{bmatrix} \cos[(m_2 - m_1)\psi + 2(\sigma_2 - \sigma_1)] & -\sin[(m_2 - m_1)\psi + 2(\sigma_2 - \sigma_1)] \\ \sin[(m_2 - m_1)\psi + 2(\sigma_2 - \sigma_1)] & \cos[(m_2 - m_1)\psi + 2(\sigma_2 - \sigma_1)] \end{bmatrix},$$

$$(19)$$

in which $\alpha = m\psi + 2\sigma$. It can be found from the expression that the combined Jones matrix is a rotation matrix, and the polarization direction of a linearly polarized beam through the device can rotate at an angle of $(m_2 - m_1)\psi + 2(\sigma_2 - \sigma_1)$ anticlockwise. The cascaded device can be transformed into a VHP by the 0° HP with the Jones matrix J_0, i.e., VHP(0, 0). The Jones matrix of the transformation process can be expressed as

$$(J_2 \cdot J_1) \cdot J_0 = \begin{bmatrix} \cos(\alpha_2 - \alpha_1) & -\sin(\alpha_2 - \alpha_1) \\ \sin(\alpha_2 - \alpha_1) & \cos(\alpha_2 - \alpha_1) \end{bmatrix}$$
$$\cdot \begin{bmatrix} \cos 0 & \sin 0 \\ \sin 0 & -\cos 0 \end{bmatrix}$$
$$= \begin{bmatrix} \cos(\alpha_2 - \alpha_1 + 0) & \sin(\alpha_2 - \alpha_1 + 0) \\ \sin(\alpha_2 - \alpha_1 + 0) & -\cos(\alpha_2 - \alpha_1 + 0) \end{bmatrix}.$$
(20)

Taking the combination of the first-order and third-order VHPs with $\sigma = 0$, for example, when passing through the 0° HP, first-order and third-order VHPs successively, the combination result is equivalent to the VHP(2, 0). And when passing through the 0° HP, third-order and first-order VHPs in turn, the cascaded one corresponds to the VHP(–2, 0). The negative sign indicates that the fast axis of the VHP changes continuously clockwise. In particular, when 0° HP is placed between the two VHPs, the VHP(4, 0) is formed. The combined Jones matrix of three VHPs can be expressed as

$$J_3 \cdot (J_2 \cdot J_1) = \begin{bmatrix} \cos(\alpha_3 - \alpha_2 + \alpha_1) & \sin(\alpha_3 - \alpha_2 + \alpha_1) \\ \sin(\alpha_3 - \alpha_2 + \alpha_1) & -\cos(\alpha_3 - \alpha_2 + \alpha_1) \end{bmatrix}.$$
(21)

It can be found from the expression that the cascaded device forms the new VHP with $m = m_3 - m_2 + m_1$. Taking the $\sigma = 0$ VHPs with $m = 2$, 3, and 7, for example, the VHPs with $m = \pm 1$, –2, –3, ± 4, ± 5, 6, –7, 8, 9, and 10 can be generated by cascading two or three of the VHPs, in which 0° HP can be placed when necessary. Similarly, the combination of five VHPs can form the new VHP with $m = m_5 - m_4 + m_3 - m_2 + m_1$. By analogy, more types of VHPs can be generated.

3. EXPERIMENTAL SETUP

Figure 3 shows the direct-view experimental setup for concise and efficient generation of arbitrary CV beams by a VHP without beam reflection and deflection. The incident beam from a linearly polarized He–Ne laser is expanded six times by two well-aligned lenses. The combination of HP1 and Gran Taylor prism (GTP) can modulate the incident beam intensity and make sure the incident beam is horizontally linearly
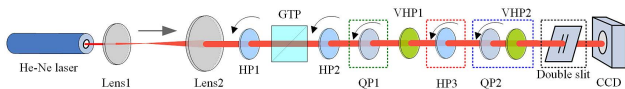
polarized, and the HP2 is used to change the linearly polarized direction. The QP1 in the green dashed line can be used to convert the linearly polarized beam into a circularly polarized beam when necessary. The HP3 in the red dashed line can be used to convert the RP or AP beam into the ARP or AAP mode polarized. And the QP2 can convert the circularly polarized beam into linearly polarized; combined with VHP2 in the blue dashed line, it helps to generate CVV beams.
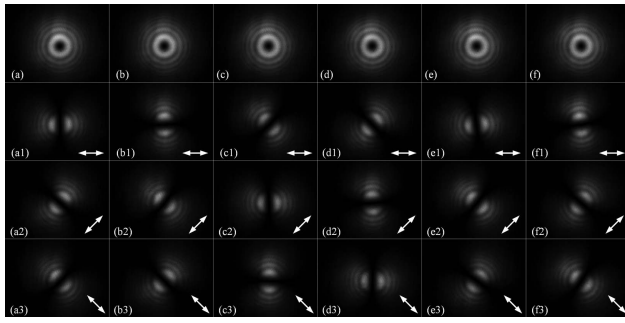
The components in the dashed lines can be arranged or not according to the beams needed, and the HPs and QPs can be rotated accordingly. Multiple types of first-order or higher-order CV beams, such as the RP, AP, and $\pi/4$-CV beams, can be generated by rotating the HP2 when there are no components in the dashed lines. When only the HP3 in the red dashed line is added to the experimental setup, the ARP and AAP beams can be generated by rotating the HP3. When only the QP1 in the green dashed line is added to the experimental setup, the linearly polarized beam is converted into a circularly polarized beam, and after passing through the VHP1, a vortex beam with circular polarization is obtained. Meanwhile, if QP2 and VHP2 in the blue dashed line are added to the experimental setup, the CVV beam can be generated.

The intensity distribution of the generated beam is captured by the CCD camera, which is a Manta G-033B modal 8-bit product of AVT Company with the resolution of 656 pixels × 492 pixels and a pixel pitch of 9.9 μm × 9.9 μm. A double slit with the slit width of 99 μm and slit spacing of 1 mm in the black dashed line can be placed in front of the camera to help detect the generated CV beams.

In the experimental setup, the VHP is supplied by LBTEK (Changsha Lubang Photonics Technology Co., Ltd.), which is a liquid crystal polymer wave plate with a fast axis rotating continuously along an azimuthal coordinate, whose function resembles the general q-plate [91–94] and S-wave plate [95–97]. The general q-plate is essentially a thin (nematic) liquid crystal film sandwiched between two coated plane glasses, which needs extra electric or temperature control. And the S-wave plate, a kind of metasurface, is a nanosubwavelength periodic structure applied in the visible region, usually written inside a glass plate by femtosecond laser, behaving as a uniaxial crystal with the optical axes parallel and perpendicular to the subwavelength grooves. These devices are characterized by singular optic axis distributions with topological charge q and are commonly called by the joint name q-plates [98,99].

4. RESULTS AND DISCUSSION

The first-order CV beams corresponding to the Jones vector of E_{RP}, E_{AP}, $E_{\pi/4}^1$, and $E_{-\pi/4}^1$ are obtained when the HP2 with the fast axis is orientated at 0°, –90°, –22.5°, and 22.5° direction, respectively, and the VHP1(1, 0) is placed in the experimental setup without components in the dashed lines. The corresponding experimental results captured by the CCD are depicted in Figs. 4(a)–4(d). The first-order ARP and AAP mode polarized beams can be obtained when the HP3 in the red dashed line with the fast axis orientated at 0° and 22.5°, respectively, passed by the RP beam is placed in the setup. The corresponding experimental results are depicted in Figs. 4(e) and 4(f). Figures 4(a1)–4(f3) are the intensity distributions after

Fig. 3. Direct-view experimental setup for the generation and double-slit interference of CV beams. Lenses 1 and 2 constitute a beam expander; HP, half-wave plate; GTP, Gran Taylor prism; QP, quarter-wave plate; VHP, vortex half-wave plate.

Fig. 4. Intensity distributions of generated first-order CV beams. (a)–(f) $E_{RP}, E_{AP}, E^1_{\pi/4}, E^1_{-\pi/4}, E_{ARP}, E_{AAP}$. Arrow heads represent the transmission direction of the polarizers.

Fig. 5. Polarization azimuth distributions of generated first-order CV beams. (a)–(f) $E_{RP}, E_{AP}, E^1_{\pi/4}, E^1_{-\pi/4}, E_{ARP}, E_{AAP}$. Arrow heads represent the polarization direction.

passing through a linear polarizer with the polarization direction orientated at 0°, 45°, and –45°, respectively, and the arrow heads indicate the transmission direction of the polarizers.

In order to get the spatial polarization distributions of generated beams, Stokes parameters S_0, S_1, S_2, and S_3 are measured by the combination of a polarizer and a QP in the following equation:

$$\begin{cases} S_0 = I_x + I_y = I_{\pi/4} + I_{-\pi/4} = I_R + I_L = I_0 \\ S_1 = I_x - I_y = S_0 - 2I_y = 2I_x - S_0 \\ S_2 = I_{\pi/4} - I_{-\pi/4} = S_0 - 2I_{-\pi/4} = 2I_{\pi/4} - S_0 \\ S_3 = I_R - I_L = S_0 - 2I_L = 2I_R - S_0 \end{cases}, \quad (22)$$

where I_0 is the total transverse intensity of the beam. I_x, I_y, $I_{\pi/4}$, and $I_{-\pi/4}$ are the transmission intensity after a polarizer with polarization direction orientated at 0°, 90°, 45°, and –45°, respectively. I_R means the right-handed circularly polarized component, which is the transmission intensity after a QP with the fast axis orientated at 0° (or 45°) and a polarizer with polarization direction orientated at 45° (or 90°) successively. Accordingly, I_L means the left-handed circular component. It is the transmission intensity after a 0° (or 45°) QP and a –45° (or 0°) polarizer successively. According to Eq. (22), Stokes parameters can be obtained only by measuring four intensities of I_0, I_x, $I_{\pi/4}$, and I_R.

Polarization parameters, including DOP, polarization azimuth (PA), and polarization ellipticity (PE), can be obtained by the following:

$$\begin{cases} p = \frac{\sqrt{S_1^2 + S_2^2 + S_3^2}}{S_0} \\ \psi = \frac{1}{2} \arctan(S_2/S_1) \\ \chi = \frac{1}{2} \arcsin \frac{S_3}{\sqrt{S_1^2 + S_2^2 + S_3^2}} \end{cases}, \quad (23)$$

where p is the DOP, ψ is the PA, and χ is the ellipsoidal polarization angle, i.e., PE. Tan(χ) represents the ratio of short axis to long axis of elliptically polarized beam. $\chi = 0°$ means the linearly polarized beam, and $\chi = \pm 45°$ means the right-handed and left-handed circularly polarized beam, respectively.

The PA distributions of generated first-order CV beams are depicted in Fig. 5. It is easy to find that the experimental results are well consistent with the theoretical ones described in Fig. 2.
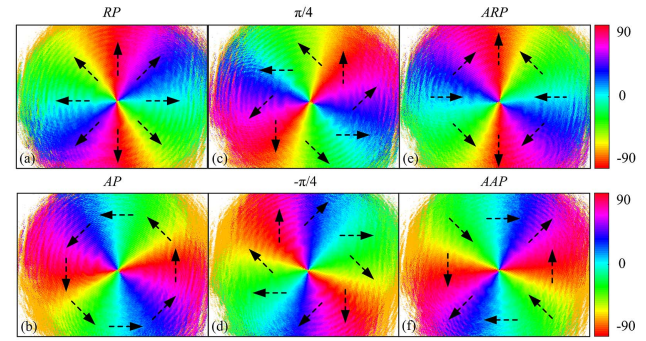
The high-order CV beams can be obtained when the VHP1 with $m \geq 2$ is placed in the experimental setup. The second-order and third-order RP beams are obtained for the VHP1(2, 0) and VHP1(3, 0) when the fast axis of HP2 is orientated at 0°. And the second-order and third-order AP beams are obtained for the VHP1(2, 0) and VHP1(3, 0) when the fast axis of HP2 is orientated at –45°. The corresponding measured Stokes and polarization parameters of generated second-order and third-order CV beams are depicted in Fig. 6. It is found that the DOP is basically equal to 1 in space as it is linearly polarized, which is demonstrated by nearly 0 of PE, and the PA is in good agreement with the theory. The experimental
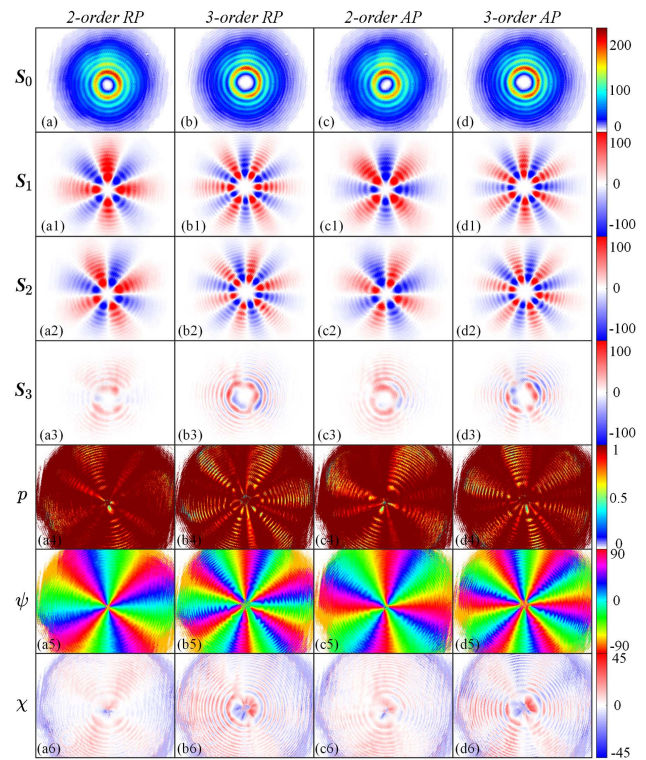

Fig. 6. Stokes parameters and polarization parameters of generated second-order and third-order CV beams. (a), (b) Second-order and third-order RP beams; (c), (d) second-order and third-order AP beams. 1–6: S_1, S_2, S_3, DOP, PA, PE.

results show that the high-order CV beams with high quality are well generated.

Vortex beams can be obtained when the QP1 in the green dashed line is added to the setup. CLCV beams are obtained when the fast axis of QP1 is orientated at 45°. The CLCV beams with topological charge number $l = 1, 2, 3$ (i.e., first-order to third-order CLCV) are obtained for the VHP1 with $m_1 = 1, 2, 3$, respectively. And anti-clockwise right-handed circularly-polarized vortex (ARCV) beams are obtained for the QP1 with the fast axis at −45°. The corresponding experimental results of first-order and third-order ARCV and CLCV beams are depicted in Fig. 7. In terms of intensity, vortex beams are hollow beams just like CV beams, but according to the PE, the polarization state is the same in the whole space, either right-handed or left-handed circular polarization. As shown in Figs. 7 (a1)–7(d1), the PA distribution is relatively random because of circular polarization.

However, from the intensity and polarization information it is hard to get the topological charge number l of vortex beams, which can be measured by the double-slit interference experiment. The experimental results of double-slit interference of first-order to third-order ARCV and CLCV beams are shown in Fig. 8. It is found that the interference fringe tilt appears, and fringes for anti-clockwise vortex beams (i.e., positive topological charge number) curve to the right, while those for clockwise ones (i.e., negative topological charge number) curve to the left. And the tilt offset increases with the increase of the topological charge number l.

The specific tilt offsets are measured by pixel positions $p_1 – p_6$ with equal transverse fringes. There are 10 fringes between p_1 and p_3 because of relatively little offset for $l = 1, 2$ shown in Figs. 8(a), 8(b), 8(d), and 8(e), and 8 fringes for $l = 3$ shown in Figs. 8(c) and 8(f). To ensure the relative accuracy of measurement, p_1 to p_3 are selected at the same ordinate $y = 50$. And p_4 to p_6, selected at the same ordinate $y = 450$, are on the same stripe as p_1 to p_3, respectively. The measured values are shown in Table 1. The fringe spacing d_0 is obtained by $d_0 = (p_3 - p_1 + p_6 - p_4)/(2N)$, in which N is the fringe number between p_1 (or p_4) and p_3 (or p_6). The fringe offset d is obtained by $d = (p_4 - p_1 + p_5 - p_2 + p_6 - p_3)/3$, and the relative offset coefficient R is defined as the ratio of d to d_0, i.e., $R_i = d_i/d_0$ $(i = -2, -1, 0, 1, 2...)$.
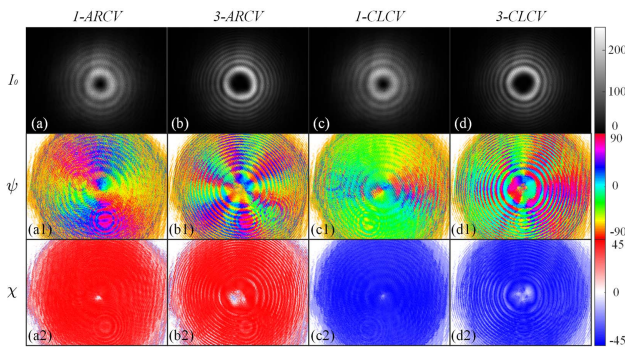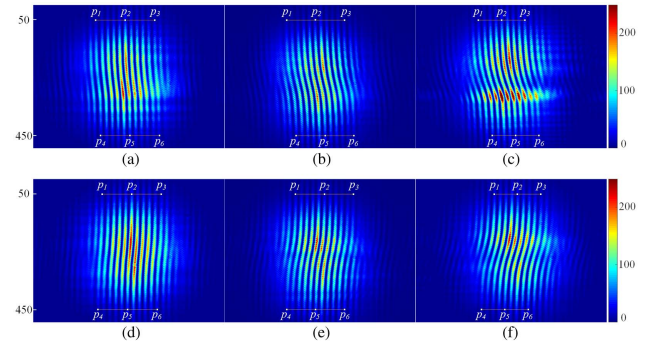
Fig. 8. Experimental results of double-slit interference of first-order to third-order ARCV and CLCV beams. (a)–(c) First-order to third-order ARCV beams; (d)–(f) first-order to third-order CLCV beams; $p_1 – p_3$, horizontal pixel positions with equal transverse fringes at $y = 50$; $p_4 – p_6$, corresponding horizontal pixel positions with equal transverse fringes at $y = 450$.

Theoretically, the relative offset coefficient R_i should be an integer equal to the topological charge l_i if the double-slit spacing is close to 0 and the beam size approaches infinity. However, due to the existence of double slit spacing and limited beam size, the two-slit phase difference of the top part of the double slit is not 0, and the one of the bottom part of the double slit is less than $2l\pi$, in which l is the topological charge number, so the phase difference of the top and bottom parts of the double slit is less than $2l\pi$, i.e., the offset of interference fringes is less than l fringes. But, the ratio of R_i of vortex beam with $l = i$ to R_1 (or $|R_{-1}|$ for $l < 0$) is close to the topological charge l, which could be expressed as follows:

$$\begin{cases} l = R_i/R_1, & l > 0 \\ l = R_i/|R_{-1}|, & l < 0 \end{cases}. \tag{24}$$

The topological charge l can be calculated based on Eq. (24). The corresponding measurement results are listed in Table 1. It is found that the measured results are in good agreement with the theoretical values except for a little deviation, which can be improved by increasing the camera pixels and reducing the pixel size.

The double-slit interference experiment is applied to the high-order CV (HCV) beams, and the corresponding experimental results of first-order to third-order CV beams are depicted in Fig. 9. It is found that misplacements appear in the double-slit interference fringes of the HCV beams, in which the misplacement region number m in a fringe is $2P + 1$ for $P \le 2$ and $2P - 1$ for $P \ge 3$, where P is the polarization order number. And the intensity distributions of double-slit interference fringes are the same for the same polarization order but different types of CV beams because of the overall symmetrical polarization distribution. For instance, Figs. 9(b) and 9(c) show the interference fringe distributions of second-order $\pi/4$ beam and the third-order AP beam, respectively, which have the same distribution as the second-order and third-order RP beams. Besides, no tilt appears according to the red vertical line in the Fig. 9.
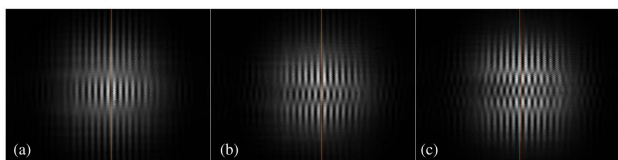
In theory, the misplacement region number M should be equal to $2P + 1$ in the condition that the double-slit spacing

Fig. 7. Intensity and polarization distributions of generated first-order and third-order ARCV and CLCV beams. (a), (b) First-order and third-order ARCV beams; (c), (d) first-order and third-order CLCV beams; I_0, intensity; ψ, PA; χ, PE.

Table 1.   Measured Values of Pixel Positions and Topological Charge Number

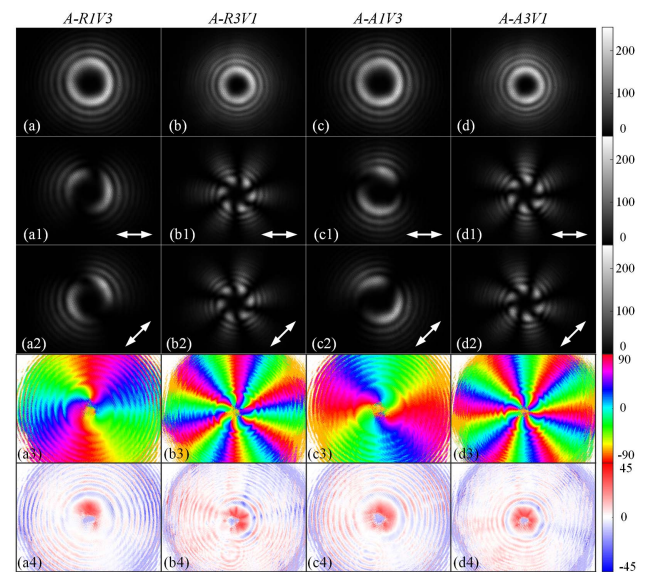| Figure	p_1	p_2	p_3	p_4	p_5	p_6	N	d_0	d	$R = d/d_0$	l
8(a)	217	318	418	233	334	434	10	20.1	16	0.7960	1
8(b)	211	312	411	243	345	444	10	20.05	32.6667	1.6293	2.0467
8(c)	217	297	376	265	345	425	8	19.9375	48.3333	2.4242	3.0454
8(d)	240	340	440	224	325	424	10	20	−15.6667	−0.7833	−1
8(e)	246	346	445	213	314	413	10	19.95	−32.3333	−1.6207	−2.069
8(f)	275	354	433	227	306	386	8	19.8125	−47.6667	−2.4059	−3.0713

is rather small (approximately 0). However, with the increase of the polarization number P, the polarization information of the HCV beam at the top and bottom of the double slit is masked because of non-zero double-slit spacing, and then misplacement regions reduce two parts. In this experiment, the missing appeared in the HCV beam with $P \geq 3$. If the double-slit spacing becomes larger, the missing may happen in the second-order CV beam. Similarly, if the spacing becomes smaller, the missing will be delayed to a higher-order CV beam. As shown in Fig. 9, although the fringe distributions of second-order and third-order CV beams both have five layers, their distribution density in the middle region is different. The higher the polarization order is, the denser the layers are.

Further, the CV vortex (CVV) beams are generated when the QP2 with the fast axis at 45° or –45° [QP2(45°) or QP2(-45°) for short in the following] and VHP2 in the blue dashed line are added to the experimental setup. According to the Section 2.D, the QP2 converts the ARCV or CLCV beam into an LV beam, and after passing through the VHP2 a CVV beam is generated. The anti-clockwise radially polarized vortex (A-RPV) beam with first-order polarization and third-order topological charge number (A-R1V3 for short) is obtained when QP1(-45°), VHP1(3,0), QP2(-45°), and VHP2(1,0) are added in the setup. Accordingly, the A-R3V1 beam is generated for QP1(-45°), VHP1(1,0), QP2(-45°), and VHP2(3,0). Also, the anti-clockwise azimuthally polarized vortex (A-APV) beam with first-order polarization and third-order topological charge number (A-A1V3 for short) is obtained when QP1(-45°), VHP1(3,0), QP2(45°), and VHP2(1,0) are added in the setup. And the A-A3V1 is generated for QP1(-45°), VHP1(1,0), QP2(45°), and VHP2(3,0). The corresponding experimental results captured by the CCD are depicted in Figs. 10(a)–10(d). Figures 10(a1)–10(d2) are the intensity distributions after passing through a 0° and 45° linear polarizer respectively. Figures 10(a3)–10(d4) are the polarization parameters of PA and PE respectively. The experimental results demonstrate that the anti-clockwise CVV (A-CVV) beams are well generated. Compared with the CV beams in Figs. 4–6, there is

a sense of clockwise rotation in the central part, either for the intensity distribution after a polarizer or for the PA distribution. However, it is hard to get the topological charge number except the polarization information. Besides, from the PE in Figs. 10(a4)–10(d4), it is found that the middle parts of the generated CVV beams are right-handed circularly-polarized beam, which comes from the ARCV beam.

Similarly, the clockwise radially polarized vortex (C-RPV) beam with first-order polarization and third-order topological charge number (C-R1V3 for short) is obtained when QP1 (45°), VHP1(3,0), QP2(-45°), and VHP2(1,0) are added in the setup. Accordingly, the C-R3V1 beam is generated for QP1(45°), VHP1(1,0), QP2(-45°), and VHP2(3,0). Also, the clockwise azimuthally polarized vortex (C-APV) beam with first-order polarization and third-order topological charge number (A-A1V3 for short) is obtained when QP1(45°), VHP1(3,0), QP2(45°), and VHP2(1,0) are added in the setup. And the C-A3V1 is generated for QP1(45°), VHP1(1,0), QP2(45°), and VHP2(3,0). The corresponding Stokes and polarization parameters of generated clockwise CVV (C-CVV) beams are depicted in Fig. 11. There is a sense of anti-clockwise rotation in the central part, either for the intensity distribution after a polarizer or for the PA distribution. And, from the PE in Figs. 11(a4)–11(d4), the middle parts of the generated CVV beams are

Fig. 9.   Experimental results of double-slit interference of first-order to third-order CV beams. (a)–(c) First-order RP beam; second-order $\pi/4$ beam; third-order AP beam.

Fig. 10.   Experimental results of generated A-CVV beams. (a)–(d) Intensities of A-R1V3, A-R3V1, A-A1V3, and A-A3V1 beams; 1, intensity after a 0° polarizer; 2, intensity after a 45° polarizer; 3, PA; 4, PE. Arrow heads indicate the transmission direction of the polarizers.
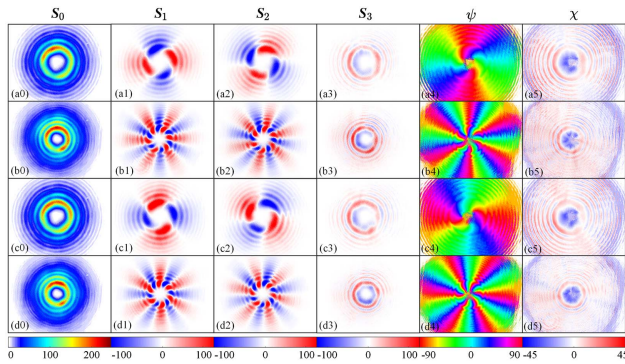
Fig. 11. Stokes parameters and polarization parameters of generated C-CVV beams. (a)–(d) C-R1V3, C-R3V1, C-A1V3, and C-A3V1 beams; 0–5: S_0, S_1, S_2, S_3, PA, PE.
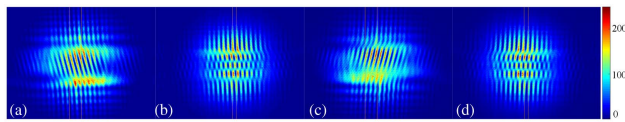
Fig. 12. Experimental results of double-slit interference of anti-clockwise and clockwise CVV beams. (a)–(d) A-R1V3 beam, A-A3V1 beam, C-A1V3 beam, and C-R3V1 beam.

left-handed circularly-polarized beam, which comes from the CLCV beam. Also, it is hard to get the topological charge number except the polarization information.

The double-slit interference experiment is also introduced to the CVV beams to help detection, and the corresponding experimental results of anti-clockwise and clockwise CVV beams are depicted in Fig. 12. Both misplacement and tilt appear, which have the same rules as CV beams in Fig. 9 and vortex beams in Fig. 8, respectively. The misplacement region number M is related to the polarization order number P, and the fringe tilt offset is related to the topological charge number l. The fringe intensity distributions of the same P and l but different types of CVV beams are the same. And A-CVV beams curve to the right and C-CVV beams curve to the left.

The topological charge number l is calculated by measuring the tilt offset. The specific measurement process is the same as that of vortex beam. As shown in Fig. 12, the tilt offset between two red vertical lines of A-R1V3 beam is three times of that of A-A3V1 beam, and C-A1V3 beam has three times the offset of C-R3V1, i.e., $l = 3$ for A-R1V3, and $l = -3$ for C-R3V1 beam.

5. CONCLUSION

In summary, we have demonstrated a concise efficient and practical direct-view method to generate arbitrary CV beams by VHP, including realizing CV beams, vortex beams and CVV beams. The characteristics of VHP are analyzed in detail. New types of VHPs can be formed by cascading two or more VHPs when the types of available VHPs are limited, which helps to generate multi-type CV beams more flexibly. Six kinds of first-order and other high-order CV beams, such as the RP beam,

AP beam, and third-order AP beam, are formed by simply rotating an HP. The Stokes parameters and double-slit interference of multi-type CV beams are investigated in detail. The polarization parameters, including DOP, polarization azimuth, and ellipticity, are obtained, which demonstrates the efficient generation of CV beams.

In addition, misplacement and tilt appear in the double-slit interference fringes of the CVV beams, in which the misplacement number M is $2P + 1$ for $P \leq 2$ and $2P - 1$ for $P \geq 3$, where P is the polarization order number, and the fringe tilt offset is positively related to the topological charge number l of CVV beams. It is experimentally demonstrated that arbitrary CV beams with high quality are effectively achieved by the proposed setup, and the double-slit interference method can be utilized to determine and analyze CV beams rapidly and concisely by practical performance, which shows its potential to be implemented as a commercial device.

Disclosures. The authors declare no conflicts of interest.

REFERENCES

1. Q. Zhan, "Cylindrical vector beams: from mathematical concepts to applications," Adv. Opt. Photon. **1**, 1–57 (2009).
2. U. Levy, Y. Silberberg, and N. Davidson, "Mathematics of vectorial Gaussian beams," Adv. Opt. Photon. **11**, 828–891 (2019).
3. K. S. Youngworth and T. G. Brown, "Focusing of high numerical aperture cylindrical-vector beams," Opt. Express **7**, 77–87 (2000).
4. R. Dorn, S. Quabis, and G. Leuchs, "Sharper focus for a radially polarized light beam," Phys. Rev. Lett. **91**, 233901 (2003).
5. C. Ping, C. Liang, F. Wang, and Y. Cai, "Radially polarized multi-Gaussian Schell-model beam and its tight focusing properties," Opt. Express **25**, 32475–32490 (2017).
6. W. Chen and Q. Zhan, "Three-dimensional focus shaping with cylindrical vector beams," Opt. Commun. **265**, 411–417 (2006).
7. E. Otte, K. Tekce, and C. Denz, "Tailored intensity landscapes by tight focusing of singular vector beams," Opt. Express **25**, 20194–20201 (2017).
8. H.-F. Xu, Y. Zhou, H.-W. Wu, H.-J. Chen, Z.-Q. Sheng, and J. Qu, "Focus shaping of the radially polarized Laguerre-Gaussian-correlated Schell-model vortex beams," Opt. Express **26**, 20076–20088 (2018).
9. H.-F. Xu, R. Zhang, Z.-Q. Sheng, and J. Qu, "Focus shaping of partially coherent radially polarized vortex beam with tunable topological charge," Opt. Express **27**, 23959–23969 (2019).
10. C. Varin and M. Piché, "Acceleration of ultra-relativistic electrons using high-intensity TM$_{01}$ laser beams," Appl. Phys. B **74**, s83–s88 (2002).
11. Q. Zhan, "Trapping metallic Rayleigh particles with radial polarization," Opt. Express **12**, 3377–3382 (2004).
12. Y. Kozawa and S. Sato, "Optical trapping of micrometer-sized dielectric particles by cylindrical vector beams," Opt. Express **18**, 10828–10833 (2010).
13. B. J. Roxworthy and K. C. Toussaint, "Optical trapping with π-phase cylindrical vector beams," New J. Phys. **12**, 073012 (2010).

14. O. M. Maragò, P. H. Jones, P. G. Gucciardi, G. Volpe, and A. C. Ferrari, "Optical trapping and manipulation of nanostructures," Nat. Nanotechnol. **8**, 807–819 (2013).

15. V. G. Niziev and A. V. Nesterov, "Influence of beam polarization on laser cutting efficiency," J. Phys. D **32**, 1455–1461 (1999).

16. M. Meier, V. Romano, and T. Feurer, "Material processing with pulsed radially and azimuthally polarized laser radiation," Appl. Phys. A **86**, 329–334 (2007).

17. M.-Q. Cai, P.-P. Li, D. Feng, Y. Pan, S.-X. Qian, Y. Li, C. Tu, and H.-T. Wang, "Microstructures fabricated by dynamically controlled femtosecond patterned vector optical fields," Opt. Lett. **41**, 1474–1477 (2016).

18. P. Török and P. Munro, "The use of Gauss-Laguerre vector beams in STED microscopy," Opt. Express **12**, 3605–3617 (2004).

19. S. Segawa, Y. Kozawa, and S. Sato, "Resolution enhancement of confocal microscopy by subtraction method with vector beams," Opt. Lett. **39**, 3118–3121 (2014).

20. Y. Kozawa and S. Sato, "Numerical analysis of resolution enhancement in laser scanning microscopy using a radially polarized beam," Opt. Express **23**, 2076–2084 (2015).

21. S. Berg-Johansen, F. Töppel, B. Stiller, P. Banzer, M. Ornigotti, E. Giacobino, G. Leuchs, A. Aiello, and C. Marquardt, "Classically entangled optical beams for high-speed kinematic sensing," Optica **2**, 864–868 (2015).

22. S. Roy, K. Ushakova, Q. van den Berg, S. F. Pereira, and H. P. Urbach, "Radially polarized light for detection and nanolocalization of dielectric particles on a planar substrate," Phys. Rev. Lett. **114**, 103903 (2015).

23. M. Neugebauer, P. Woźniak, A. Bag, G. Leuchs, and P. Banzer, "Polarization-controlled directional scattering for nanoscopic position sensing," Nat. Commun. **7**, 11286 (2016).

24. G. Milione, T. A. Nguyen, J. Leach, D. A. Nolan, and R. R. Alfano, "Using the nonseparability of vector beams to encode information for optical communication," Opt. Lett. **40**, 4887–4890 (2015).

25. G. Milione, M. P. J. Lavery, H. Huang, Y. Ren, G. Xie, T. A. Nguyen, E. Karimi, L. Marrucci, D. A. Nolan, R. R. Alfano, and A. E. Willner, "4 × 20 gbit/s mode division multiplexing over free space using vector modes and a *q*-plate mode (de)multiplexer," Opt. Lett. **40**, 1980–1983 (2015).

26. Y. Zhao and J. Wang, "High-base vector beam encoding/decoding for visible-light communications," Opt. Lett. **40**, 4843–4846 (2015).

27. X.-L. Wang, X.-D. Cai, Z.-E. Su, M.-C. Chen, D. Wu, L. Li, N.-L. Liu, C.-Y. Lu, and J.-W. Pan, "Quantum teleportation of multiple degrees of freedom of a single photon," Nature **518**, 516–519 (2015).

28. P. Li, B. Wang, and X. Zhang, "High-dimensional encoding based on classical nonseparability," Opt. Express **24**, 15143–15159 (2016).

29. A. Sit, F. Bouchard, R. Fickler, J. Gagnon-Bischoff, H. Larocque, K. Heshami, D. Elser, C. Peuntinger, K. Günthner, B. Heim, C. Marquardt, G. Leuchs, R. W. Boyd, and E. Karimi, "High-dimensional intracity quantum cryptography with structured photons," Optica **4**, 1006–1010 (2017).

30. J. Zhu, Y. Chen, Y. Zhang, X. Cai, and S. Yu, "Spin and orbital angular momentum and their conversion in cylindrical vector vortices," Opt. Lett. **39**, 4435–4438 (2014).

31. S. Fu, C. Guo, G. Liu, Y. Li, H. Yin, Z. Li, and Z. Chen, "Spin-orbit optical Hall effect," Phys. Rev. Lett. **123**, 243904 (2019).

32. P. Shi, L. Du, and X. Yuan, "Structured spin angular momentum in highly focused cylindrical vector vortex beams for optical manipulation," Opt. Express **26**, 23449–23459 (2018).

33. Y. Han, L. Chen, Y.-G. Liu, Z. Wang, H. Zhang, K. Yang, and K. C. Chou, "Orbital angular momentum transition of light using a cylindrical vector beam," Opt. Lett. **43**, 2146–2149 (2018).

34. M. Li, Y. Cai, S. Yan, Y. Liang, P. Zhang, and B. Yao, "Orbit-induced localized spin angular momentum in strong focusing of optical vectorial vortex beams," Phys. Rev. A **97**, 053842 (2018).

35. S. N. Khonina, A. V. Ustinov, and S. A. Degtyarev, "Inverse energy flux of focused radially polarized optical beams," Phys. Rev. A **98**, 043823 (2018).

36. S. Degtyarev, D. Savelyev, S. Khonina, and N. Kazanskiy, "Metasurfaces with continuous ridges for inverse energy flux generation," Opt. Express **27**, 15129–15135 (2019).

37. A. Yanai, M. Grajower, G. M. Lerman, M. Hentschel, H. Giessen, and U. Levy, "Near- and far-field properties of plasmonic oligomers under radially and azimuthally polarized light excitation," ACS Nano **8**, 4969–4974 (2014).

38. S. A. Syubaev, A. Y. Zhizhchenko, D. V. Pavlov, S. O. Gurbatov, E. V. Pustovalov, A. P. Porfirev, S. N. Khonina, S. A. Kulinich, J. B. B. Rayappan, S. I. Kudryashov, and A. A. Kuchmizhak, "Plasmonic nanolenses produced by cylindrical vector beam printing for sensing applications," Sci. Rep. **9**, 19750 (2019).

39. S. A. Schulz, T. Machula, E. Karimi, and R. W. Boyd, "Integrated multi vector vortex beam generator," Opt. Express **21**, 16130–16141 (2013).

40. X. Ma, S. Zheng, Q. Chen, S. Tan, P. Zhang, Q. Lu, J. Wang, and W. Guo, "High-speed directly modulated cylindrical vector beam lasers," ACS Photon. **6**, 3261–3270 (2019).

41. L. Feng, Y. Li, S. Wu, X. Guan, C. Yang, W. Tong, W. Li, J. Qiu, X. Hong, Y. Zuo, H. Guo, E. Chen, and J. Wu, "All-fiber generation of arbitrary cylindrical vector beams on the first-order Poincaré sphere," Photon. Res. **8**, 1268–1277 (2020).

42. Y. Sebbag and U. Levy, "Arbitrarily directed emission of integrated cylindrical vector vortex beams by geometric phase engineering," Opt. Lett. **45**, 6779–6782 (2020).

43. K. Yonezawa, Y. Kozawa, and S. Sato, "Generation of a radially polarized laser beam by use of the birefringence of a *c*-cut Nd:YVO$_4$ crystal," Opt. Lett. **31**, 2151–2153 (2006).

44. G. Machavariani, Y. Lumer, I. Moshe, A. Meir, S. Jackel, and N. Davidson, "Birefringence-induced bifocusing for selection of radially or azimuthally polarized laser modes," Appl. Opt. **46**, 3304–3310 (2007).

45. K. Yonezawa, Y. Kozawa, and S. Sato, "Compact laser with radial polarization using birefringent laser medium," Jpn. J. Appl. Phys. **46**, 5160–5163 (2007).

46. J. F. Bisson, J. Li, K. Ueda, and Y. Senatsky, "Radially polarized ring and arc beams of a neodymium laser with an intra-cavity axicon," Opt. Express **14**, 3304–3311 (2006).

47. Y. Kozawa and S. Sato, "Generation of a radially polarized laser beam by use of a conical Brewster prism," Opt. Lett. **30**, 3063–3065 (2005).

48. S. Vyas, Y. Kozawa, and S. Sato, "Generation of radially polarized Bessel–Gaussian beams from *c*-cut Nd:YVO$_4$ laser," Opt. Lett. **39**, 1101–1104 (2014).

49. D. Naidoo, F. S. Roux, A. Dudley, I. Litvin, B. Piccirillo, L. Marrucci, and A. Forbes, "Controlled generation of higher-order Poincaré sphere beams from a laser," Nat. Photonics **10**, 327–332 (2016).

50. G. Machavariani, Y. Lumer, I. Moshe, A. Meir, and S. Jackel, "Efficient extracavity generation of radially and azimuthally polarized beams," Opt. Lett. **32**, 1468–1470 (2007).

51. W. J. Lai, B. C. Lim, P. B. Phua, K. S. Tiaw, H. H. Teo, and M. H. Hong, "Generation of radially polarized beam with a segmented spiral varying retarder," Opt. Express **16**, 15694–15699 (2008).

52. J. Qi, H. Zhang, B. Pan, H. Deng, J. Yang, B. Shi, H. Wang, A. Du, W. Wang, and X. Li, "A succinct method to generate multi-type HCV beams with a spatial spiral varying retardation-plate," Europhys. Lett. **121**, 54004 (2018).

53. K. J. Moh, X.-C. Yuan, J. Bu, D. K. Y. Low, and R. E. Burge, "Direct noninterference cylindrical vector beam generation applied in the femtosecond regime," Appl. Phys. Lett. **89**, 251114 (2006).

54. S. N. Khonina, A. V. Ustinov, S. A. Fomchenkov, and A. P. Porfirev, "Formation of hybrid higher-order cylindrical vector beams using binary multi-sector phase plates," Sci. Rep. **8**, 14320 (2018).

55. C. Loussert and E. Brasselet, "Efficient scalar and vectorial singular beam shaping using homogeneous anisotropic media," Opt. Lett. **35**, 7–9 (2010).

56. T. Fadeyeva, V. Shvedov, N. Shostka, C. Alexeyev, and A. Volyar, "Natural shaping of the cylindrically polarized beams," Opt. Lett. **35**, 3787–3789 (2010).

57. S. N. Khonina, S. V. Karpeev, V. D. Paranin, and A. A. Morozov, "Polarization conversion under focusing of vortex laser beams along the axis of anisotropic crystals," Phys. Lett. A **381**, 2444–2455 (2017).

58. S. N. Khonina, A. P. Porfirev, and N. L. Kazanskiy, "Variable transformation of singular cylindrical vector beams using anisotropic crystals," Sci. Rep. **10**, 5590 (2020).

59. S. N. Khonina and S. V. Karpeev, "Generating inhomogeneously polarized higher-order laser beams by use of diffractive optical elements," J. Opt. Soc. Am. A **28**, 2115–2123 (2011).

60. S. N. Khonina, S. V. Karpeev, and A. P. Porfirev, "Sector sandwich structure: an easy-to-manufacture way towards complex vector beam generation," Opt. Express **28**, 27628–27643 (2020).

61. Z. Bomzon, G. Biener, V. Kleiner, and E. Hasman, "Radially and azimuthally polarized beams generated by space-variant dielectric subwavelength gratings," Opt. Lett. **27**, 285–287 (2002).

62. G. M. Lerman and U. Levy, "Generation of a radially polarized light beam using space-variant subwavelength gratings at 1064 nm," Opt. Lett. **33**, 2782–2784 (2008).

63. C. Zhu, Q. Jiao, X. Tan, W. Wang, and Bayanheshig, "Design of a subwavelength all-metal grating for generating azimuthally polarized beams based on modified particle swarm optimization," Appl. Opt. **58**, 4052–4058 (2019).

64. P. Yu, S. Chen, J. Li, H. Cheng, Z. Li, W. Liu, B. Xie, Z. Liu, and J. Tian, "Generation of vector beams with arbitrary spatial variation of phase and linear polarization using plasmonic metasurfaces," Opt. Lett. **40**, 3229–3232 (2015).

65. F. Yue, D. Wen, J. Xin, B. D. Gerardot, J. Li, and X. Chen, "Vector vortex beam generation with a single plasmonic metasurface," ACS Photon. **3**, 1558–1563 (2016).

66. Y. Liu, X. Ling, X. Yi, X. Zhou, H. Luo, and S. Wen, "Realization of polarization evolution on higher-order Poincaré sphere with metasurface," Appl. Phys. Lett. **104**, 191110 (2014).

67. W. Shu, Y. Liu, Y. Ke, X. Ling, Z. Liu, B. Huang, H. Luo, and X. Yin, "Propagation model for vector beams generated by metasurfaces," Opt. Express **24**, 21177–21189 (2016).

68. V. G. Niziev, R. S. Chang, and A. V. Nesterov, "Generation of inhomogeneously polarized laser beams by use of a Sagnac interferometer," Appl. Opt. **45**, 8393–8399 (2006).

69. S. Liu, P. Li, T. Peng, and J. Zhao, "Generation of arbitrary spatially variant polarization beams with a trapezoid Sagnac interferometer," Opt. Express **20**, 21715–21721 (2012).

70. P. Li, Y. Zhang, S. Liu, C. Ma, L. Han, H. Cheng, and J. Zhao, "Generation of perfect vectorial vortex beams," Opt. Lett. **41**, 2205–2208 (2016).

71. J. Jia, Z. Chang, H. Yang, Q. Liu, F. Wang, H. Gao, F. Li, and P. Zhang, "Mode sorter designed for (de)multiplexing vector vortex modes," Appl. Opt. **58**, 7094–7099 (2019).

72. X. Xu, Y. Zhou, Y.-S. Yuan, J. Wang, H.-F. Xu, and J. Qu, "Generation of cylindrical and elliptical symmetrical vector beam on the Mach–Zehnder interferometer," AIP Adv. **8**, 125007 (2018).

73. C. Chen, Y. Zhang, L. Ma, Y. Zhang, Z. Li, R. Zhang, X. Zeng, Z. Zhan, C. He, X. Ren, C. Cheng, and C. Liu, "Flexible generation of higher-order Poincaré beams with high efficiency by manipulating the two eigenstates of polarized optical vortices," Opt. Express **28**, 10618–10632 (2020).

74. S. C. Tidwell, D. H. Ford, and W. D. Kimura, "Generating radially polarized beams interferometrically," Appl. Opt. **29**, 2234–2239 (1990).

75. N. Passilly, R. de Saint Denis, K. Aït-Ameur, F. Treussart, R. Hierle, and J.-F. Roch, "Simple interferometric technique for generation of a radially polarized light beam," J. Opt. Soc. Am. A **22**, 984–991 (2005).

76. X.-L. Wang, J. Ding, W.-J. Ni, C.-S. Guo, and H.-T. Wang, "Generation of arbitrary vector beams with a spatial light modulator and a common path interferometric arrangement," Opt. Lett. **32**, 3549–3551 (2007).

77. Z. Chen, T. Zeng, B. Qian, and J. Ding, "Complete shaping of optical vector beams," Opt. Express **23**, 17701–17710 (2015).

78. J. Mendoza-Hernández, M. F. Ferrer-Garcia, J. A. Rojas-Santana, and D. Lopez-Mago, "Cylindrical vector beam generator using a two-element interferometer," Opt. Express **27**, 31810–31819 (2019).

79. W. Han, Y. Yang, W. Cheng, and Q. Zhan, "Vectorial optical field generator for the creation of arbitrarily complex fields," Opt. Express **21**, 20692–20706 (2013).

80. S. Fu, C. Gao, T. Wang, S. Zhang, and Y. Zhai, "Simultaneous generation of multiple perfect polarization vortices with selective spatial states in various diffraction orders," Opt. Lett. **41**, 5454–5457 (2016).

81. S. Fu, T. Wang, and C. Gao, "Generating perfect polarization vortices through encoding liquid-crystal display devices," Appl. Opt. **55**, 6501–6505 (2016).

82. S. Fu, C. Gao, T. Wang, Y. Zhai, and C. Yin, "Anisotropic polarization modulation for the production of arbitrary Poincaré beams," J. Opt. Soc. Am. B **35**, 1–7 (2018).

83. M. Bashkansky, D. Park, and F. K. Fatemi, "Azimuthally and radially polarized light with a nematic SLM," Opt. Express **18**, 212–217 (2010).

84. J. Qi, W. Sun, J. Liao, Y. Nie, X. Wang, J. Zhang, X. Liu, H. Jia, M. Lu, S. Chen, J. Liu, J. Yang, J. Tan, and X. Li, "Generation and analysis of both in-phase and out-phase radially polarized femtosecond-pulse beam," Opt. Eng. **45**, 024201 (2013).

85. Y. Zhang, P. Li, C. Ma, S. Liu, H. Cheng, L. Han, and J. Zhao, "Efficient generation of vector beams by calibrating the phase response of a spatial light modulator," Appl. Opt. **56**, 4956–4960 (2017).

86. S. Liu, S. Qi, Y. Zhang, P. Li, D. Wu, L. Han, and J. Zhao, "Highly efficient generation of arbitrary vector beams with tunable polarization, phase, and amplitude," Photon. Res. **6**, 228–233 (2018).

87. Y. Zhou, X. Li, Y. Cai, Y. Zhang, S. Yan, M. Zhou, M. Li, and B. Yao, "Compact optical module to generate arbitrary vector vortex beams," Appl. Opt. **59**, 8932–8938 (2020).

88. S. N. Khonina, A. V. Ustinov, and A. P. Porfirev, "Vector Lissajous laser beams," Opt. Lett. **45**, 4112–4115 (2020).

89. M. Rashid, O. M. Maragò, and P. H. Jones, "Focusing of high order cylindrical vector beams," J. Opt. A **11**, 065204 (2009).

90. S. N. Khonina, "Vortex beams with high-order cylindrical polarization: features of focal distributions," Appl. Phys. B **125**, 100 (2019).

91. L. Marrucci, C. Manzo, and D. Paparo, "Pancharatnam-Berry phase optical elements for wave front shaping in the visible domain: switchable helical mode generation," Appl. Phys. Lett. **88**, 221102 (2006).

92. E. Karimi, B. Piccirillo, E. Nagali, L. Marrucci, and E. Santamato, "Efficient generation and sorting of orbital angular momentum eigenmodes of light by thermally tuned q-plates," Appl. Phys. Lett. **94**, 231124 (2009).

93. S. Slussarenko, A. Murauski, T. Du, V. Chigrinov, L. Marrucci, and E. Santamato, "Tunable liquid crystal q-plates with arbitrary topological charge," Opt. Express **19**, 4085–4090 (2011).

94. A. Rubano, F. Cardano, B. Piccirillo, and L. Marrucci, "Q-plate technology: a progress review [Invited]," J. Opt. Soc. Am. B **36**, D70–D87 (2019).

95. M. Beresna, M. Gecevicius, P. G. Kazansky, and T. Gertus, "Radially polarized optical vortex converter created by femtosecond laser nanostructuring of glass," Appl. Phys. Lett. **98**, 201101 (2011).

96. M. Beresna, M. Gecevičius, and P. G. Kazansky, "Polarization sensitive elements fabricated by femtosecond laser nanostructuring of glass [Invited]," Opt. Mater. Express **1**, 783–795 (2011).

97. D. Wu, Y. Li, W. Jia, J. Zhou, Y. Zhao, Y. Fu, and J. Wang, "Generation of arbitrary vector vortex beams based on the dual-modulation method," Appl. Opt. **58**, 1508–1513 (2019).

98. L. Marrucci, C. Manzo, and D. Paparo, "Optical spin-to-orbital angular momentum conversion in inhomogeneous anisotropic media," Phys. Rev. Lett. **96**, 163905 (2006).

99. W. Shu, X. Ling, X. Fu, Y. Liu, Y. Ke, and H. Luo, "Polarization evolution of vector beams generated by q-plates," Photon. Res. **5**, 64–72 (2017).